The Astrophysical Journal, 806:245 (13pp), 2015 June 20 doi:10.1088/0004-637X/806/2/245

INVESTIGATION OF HELICITY AND ENERGY FLUX TRANSPORT IN THREE EMERGING SOLAR ACTIVE REGIONS

P. Vemareddy
Indian Institute of Astrophysics, II Block, Koramangala, Bangalore-560 034, India; vemareddy@iiap.res.in

Received 2015 February 27; accepted 2015 April 27; published 2015 June 22

ABSTRACT

We report the results of an investigation of helicity and energy flux transport from three emerging solar active regions (ARs). Using time sequence vector magnetic field observations obtained from the Helioseismic Magnetic Imager, the velocity field of plasma flows is derived by the differential affine velocity estimator for vector magnetograms. In three cases, the magnetic fluxes evolve to pump net positive, negative, and mixed-sign helicity flux into the corona. The coronal helicity flux is dominantly coming from the shear term that is related to horizontal flux motions, whereas energy flux is dominantly contributed by the emergence term. The shear helicity flux has a phase delay of 5–14 hr with respect to absolute magnetic flux. The nonlinear curve of coronal energy versus relative helicity identifies the configuration of coronal magnetic fields, which is approximated by a fit of linear force-free fields. The nature of coronal helicity related to the particular pattern of evolving magnetic fluxes at the photosphere has implications for the generation mechanism of two kinds of observed activity in the ARs.

Key words: Sun: corona – Sun: coronal mass ejections (CMEs) – Sun: evolution – Sun: flares – Sun: magnetic fields – Sun: photosphere

1. INTRODUCTION

It is generally believed that solar magnetic fields, together with their helicity, are created in the convection zone by various dynamo processes (Choudhuri et al. 2004; Choudhuri 2007). These fields and helicity are transported into the corona through the solar photosphere and finally released into the interplanetary space via various processes, such as coronal mass ejections (CMEs) and solar winds (Zhang & Low 2005; Zhang et al. 2013). Therefore, solar eruptive events like flares and CMEs have drawn the majority of scientific interest due to their significant impact on the space weather. After nearly four decades of research from observations (Webb & Howard 2012, and references therein) and theoretical (e.g., Klimchuk 2001; Priest & Forbes 2002; Lin et al. 2003) and numerical modeling (e.g., Forbes et al. 2006), the established view on their physical understanding is that they are magnetically driven events produced by the storage of magnetic energy and helicity in the coronal volume of space above the active regions (ARs). However, there is yet no established theory, and observational analysis has provided quantitative estimates of these terms over which an eruption can predictably occur. Therefore, the present major challenges are to determine the detailed mechanism of how the AR magnetic system stores energy and helicity and to quantify their budgets to accurate levels.

During the evolution of an AR, the fundamental processes for the storage of energy and helicity in the solar atmosphere are flux emergence and shearing of magnetic field through photospheric motions. Magnetic helicity is accumulated in the corona by shearing and braiding of magnetic field lines in the photosphere. Magnetic helicity is a metric describing the volumetric complexity of the AR magnetic field. Its transport across the solar surface can be computed (Berger & Field 1984; Finn & Antonsen 1985) by the flux

$$\left.\frac{dH}{dt}\right|_S = 2\int_S \left(\boldsymbol{A}_P \bullet \boldsymbol{B}_{\rm t}\right) V_{\perp {\rm n}} dS - 2\int_S \left(\boldsymbol{A}_P \bullet \boldsymbol{V}_{\perp {\rm t}}\right) B_{\rm n} dS \qquad (1)$$

where $\boldsymbol{A}_{\rm p}$ is the vector potential of the potential field $\boldsymbol{B}_{\rm p}$, $\boldsymbol{B}_{\rm t}$ and $B_{\rm n}$ denote the tangential and normal components of magnetic fields, respectively, and $\boldsymbol{V}_{\perp {\rm t}}$ and $\boldsymbol{V}_{\perp {\rm n}}$ are the tangential and normal components, respectively, of velocity $\boldsymbol{V}_{\perp}$, the velocity perpendicular to the magnetic field lines. It indicates that the magnetic helicity in the corona originates from two sources: the twisted magnetic flux tubes emerging from the solar interior into the corona (first term; emergence term hereafter), and by the shearing and braiding of the field lines by the tangential motions on the solar surface (second term; shear term hereafter). The magnetic energy (Poynting) flux across the surface (Kusano et al. 2002), in a similar form, can be expressed as

$$\left.\frac{dE}{dt}\right|_S = \frac{1}{4\pi}\int_S B_{\rm t}^2 V_{\perp {\rm n}} dS - \frac{1}{4\pi}\int_S \left(\boldsymbol{B}_{\rm t} \bullet \boldsymbol{V}_{\perp {\rm t}}\right) B_{\rm n} dS \qquad (2)$$

meaning that the energy flux across the solar surface comes from the emergence of twisted magnetic tubes from the solar interior (first term; emergence or $V_{\perp {\rm n}}$ term) and is generated by shearing magnetic field lines due to tangential motions on the surface (second term; shear or $V_{\perp {\rm t}}$ term). The above equations show that the computation of the helicity and energy fluxes on the Sun requires vector magnetic and velocity fields on the photosphere. Using routinely available time sequence line-of-sight (LOS) magnetic field observations, many researchers (e.g., Chae 2001; Kusano et al. 2002; Nindos et al. 2003; Pariat et al. 2005; Jeong & Chae 2007; Park et al. 2010; Vemareddy et al. 2012b) derived tangential velocities of fluxes by the local correlation tracking (LCT; November & Simon 1988) technique and estimated the shear term contribution of helicity flux. As the emergence term requires LOS velocities, deriving the emergence term is not a straightforward task, and only a few attempts have been made on these equations of helicity and energy budgets (e.g., Kusano et al. 2002; Nindos et al. 2003;

Yamamoto et al. 2005; Yamamoto & Sakurai 2009; Liu & Schuck 2012).

Démoulin & Berger (2003) have introduced flux transport velocity ($\boldsymbol{u}$) as the apparent horizontal motions, which include the effect of both the emergence ($V_{\perp \mathrm{n}}$) and shearing motions ($\boldsymbol{V}_{\perp \mathrm{t}}$),

$$\boldsymbol{u} = \boldsymbol{V}_{\perp \mathrm{t}} - \frac{V_{\perp \mathrm{n}}}{B_n}\boldsymbol{B}_t. \tag{3}$$

Using this relationship, they hypothesized that the magnetic energy and helicity fluxes in Equations (1) and (2) can be estimated only from the horizontal motions deduced by tracking the photospheric cross section of magnetic flux tubes. Admitting this assumption to be correct, in a recent study, Vemareddy et al. (2012b) compared helicity accumulation in the two ARs with the corresponding flux content. From this comparison, they inferred that the shear term contributed dominantly to the coronal helicity and concluded that horizontal flux motions played a major role in the observed eruptions in those ARs.

However, Schuck (2005) has shown that the LCT method is inconsistent with the magnetic induction equation, which governs the temporal evolution of the photospheric magnetic fields. Using an optical flow based technique, he proposed the differential affine velocity estimator for vector magnetograms (DAVE4VM; Schuck 2008) method to derive the vector velocity field using vector magnetic field observations. In the meantime, several other methods have been developed for inferring plasma velocities consistent with the induction equation at the photospheric level, based on the LOS and vector magnetograms (Kusano et al. 2002; Longcope 2004; Welsch et al. 2004). In a recent study of two emerging ARs using Helioseismic Magnetic Imager (HMI) vector magnetic field data, Liu & Schuck (2012) calculated shear and emergence terms separately and found that shear is the dominant contributor to the coronal helicity, whereas it is emergence that is the dominant contributor to the coronal energy. They also checked Démoulin & Berger's (2003) hypothesis of the equivalence between the flux transport velocity and the apparent horizontal velocity and found them to be different. Exploiting routinely available high-quality vector magnetic field data from HMI (Schou et al. 2012) and using consistent algorithms to derive velocities, we are now in a position to refine the results from previous attempts to estimate helicity and energy budgets as in Equations (1) and (2).

To revisit previous studies and to add more statistics to their results, the present study is focused on estimating energy and helicity budgets in three emerging ARs. By following the emerging ARs, it is feasible to track the complete history of flux motions to identify the nature of the evolution of the helicity and energy flux profiles since the AR appears on the solar disk. From these time profiles, one can also look for a plausible correlation between the extents of energetic and complex phases of the AR and the occurrence time of the major eruptions. We applied the same approach as in Liu & Schuck (2012) on HMI vector magnetic field observations. Mainly, our aim in this study is to quantify the timing of the overall energy and helicity budgets and in particular the relative timing of the emergence and shear fluxes in relation to the timing of the net unsigned flux. In particular, it is also the subject of this study to determine whether the emergence or shear term plays a major role in the buildup of coronal energy and helicity fluxes. In addition, we explored the relevance of the evolution of the coronal energy corresponding to the evolution of relative helicity.

The rest of this manuscript is organized as follows. In Section 2, we briefly describe the observational data along with the details of computation of energy and helicity fluxes. The results of the analysis are furnished with significant details in Sections 3–7. A discussion of these results is given in Section 8, and we conclude in Section 9 with a summary.

2. OBSERVATIONAL DATA AND COMPUTATIONAL PROCEDURE

To calculate energy and helicity fluxes, we require three components of magnetic field observations at the photospheric surface, which were obtained (data series: `hmi.sharp.cea.720s`) from the recently launched HMI on board the *Solar Dynamic Observatory* (*SDO*). HMI observes the full solar disk in the Fe I λ6173 spectral line with a spatial resolution of 0.5 arcsec pixel^{-1}. Filtergrams are obtained at six wavelength positions about the line center to compute Stokes parameters I, Q, U, and V. These are then reduced with the HMI science data processing pipeline (Hoeksema et al. 2014) to retrieve the vector magnetic field using the very fast inversion of the Stokes vector algorithm (Borrero et al. 2011; Centeno et al. 2014) based on the Milne–Eddington atmospheric model. The inherent 180° azimuthal ambiguity is resolved using the minimum energy method (Metcalf et al. 1995; Leka et al. 2009). The projection effects in the field components in the cutout area are corrected by transforming to disk center using the cylindrical equal area projection method (Calabretta & Greisen 2002; Bobra et al. 2014). Detailed documentation on the pipeline processing of HMI magnetic field data, including various data artifacts, is available in Hoeksema et al. (2014).

From these time-series (every 12 minutes) vector magnetic field data, we derived the vector velocity field by using DAVE4VM (Schuck 2008). This method estimates velocity components by constructing an affine velocity profile within a windowed region around a point and constrains that profile to satisfy the induction equation. We set the window size as 19 pixels by examining the slope, Pearson linear correlation coefficient, and Spearman rank order between $\nabla_h \bullet \left(V_{\mathrm{n}} \boldsymbol{B}_{\mathrm{t}} - \boldsymbol{V}_{\mathrm{t}} B_{\mathrm{n}} \right)$ and $\delta B_{\mathrm{n}}/\delta t$ (Schuck 2008). These velocity components are further corrected by removing the field-aligned plasma flow contribution by using the relation

$$\boldsymbol{V}_{\perp} = \boldsymbol{V} - \frac{\boldsymbol{V} \bullet \boldsymbol{B}}{B^2}\boldsymbol{B} \tag{4}$$

where $\boldsymbol{V}_{\perp}$ is the velocity perpendicular to the magnetic field line and $\boldsymbol{V}$ is the velocity derived by DAVE4VM.

The vector potential $\boldsymbol{A}_{\mathrm{p}}$ in Equation (1) can be computed from the normal component of the magnetic field as a boundary condition and by imposing a Coulomb gauge restriction (Chae 2001). Since the helicity flux density is a dependent quantity on the choice of the gauge, together with the periodic nature of the boundary normal field component implicit in the fast Fourier transform (FFT) method, the helicity flux density is found to contain incorrect signals. To reduce the severity of this problem to some extent, Pariat et al. (2005) suggest an alternative formula using relative velocities following which

Equation (1) can be reformed as

$$\begin{aligned}\left.\frac{dH}{dt}\right|_S &= \frac{1}{2\pi}\int_S\int_{S'} dS\, dS'\, \hat{\boldsymbol{n}}\bullet\frac{\boldsymbol{x}-\boldsymbol{x}'}{\left|\boldsymbol{x}-\boldsymbol{x}'\right|^2}\\ &\quad\times\left\{\boldsymbol{B}_{\rm t}(\boldsymbol{x})V_{\perp\rm n}(\boldsymbol{x})B_{\rm n}\left(\boldsymbol{x}'\right)-\boldsymbol{B}_{\rm t}\left(\boldsymbol{x}'\right)V_{\perp\rm n}\left(\boldsymbol{x}'\right)B_{\rm n}(\boldsymbol{x})\right\}\\ &\quad-\frac{1}{2\pi}\int_S\int_{S'} dS\, dS'\, \hat{\boldsymbol{n}}\bullet\frac{\boldsymbol{x}-\boldsymbol{x}'}{\left|\boldsymbol{x}-\boldsymbol{x}'\right|^2}\\ &\quad\times\left\{\left[\boldsymbol{V}_{\perp\rm t}(\boldsymbol{x})-\boldsymbol{V}_{\perp\rm t}\left(\boldsymbol{x}'\right)\right]B_{\rm n}(\boldsymbol{x})B_{\rm n}\left(\boldsymbol{x}'\right)\right\}.\end{aligned} \tag{5}$$

The difference found by Pariat et al. (2005) is due to different types of Green's functions. Recently, Liu & Schuck (2013) identified this difference as a result of inconsistent boundary conditions, and an equivalent version of helicity flux density for Equation (5) using periodic Green's function is derived:

$$G_\theta(\boldsymbol{x}) = \frac{{\rm G}_A(\boldsymbol{x})}{2} + B_{\rm n}(\boldsymbol{x})\sum_{p,q=-\infty}^{\infty} e^{i2\pi\left(\frac{px}{L_x}+\frac{qy}{L_y}\right)} \left\{\frac{i\hat{n}\bullet\left[\tilde{\boldsymbol{F}}_{pq}\times\left(\frac{2\pi p}{L_x},\frac{2\pi q}{L_y}\right)\right]}{\left(\frac{2\pi p}{L_x}\right)^2+\left(\frac{2\pi q}{L_y}\right)^2}\right\} \tag{6}$$

where the summation represents the inverse Fourier transform of the term in curly brackets. Here $G_A(\boldsymbol{x}) = -2(\boldsymbol{u}\cdot\boldsymbol{A}_{\rm p})B_{\rm n}$ includes both shear and emergence terms in Equation (1) as per Equation (3), and $\tilde{\boldsymbol{F}}_{pq}$ is the Fourier amplitude of spatial function $\boldsymbol{F}$ $(=B_{\rm n}(\boldsymbol{x})\boldsymbol{V}_{\perp\rm t}(\boldsymbol{x}) + \boldsymbol{B}_{\rm t}(x)V_{\perp\rm n} = \boldsymbol{F}_{\rm shear} + \boldsymbol{F}_{\rm adv})$ with harmonic p, q in a Fourier space with spatial dimensions L_x and L_y. We first compute the vector potential $\boldsymbol{A}_{\rm p}$ by using the normal component of the magnetic field as the boundary with a Coulomb gauge condition (Chae 2001). Then using the derived velocity field ($\boldsymbol{V}_\perp$) from observations, we compute the terms in G_A. Inserting the Fourier transformed terms of $\boldsymbol{F}$ into curly brackets and applying inverse Fourier transform yields two terms, which when added to the terms of $G_A(\boldsymbol{x})$ will result in shear and emergence terms of $G_\theta(\boldsymbol{x})$ as per Equation (6). For reducing the effect of aliasing intrinsic in the FFT algorithm, we padded the boundary condition such that its original dimensions are increased by six times (see Figure 6 of Liu & Schuck 2013), which yields the shear and advection terms as accurately as time-consuming direct integration (as used in Vemareddy et al. 2012b for shear term computation) in Equation (5) within a difference of 2% (and a correlation of 0.999). Having implemented these procedures on the data, the detailed results are discussed in the following sections.

3. AR 11560

The AR 11560 emerged with two bipolar spots on the solar disk position N3E40 on 2012 August 29. These two bipoles evolved with growing cross-sectional area at the photospheric level. While they keep growing for a day with increasing separation motion, another bipolar region emerges amid them on August 30. This configuration is similar to the famous AR 11158 (e.g., Maurya et al. 2012; Sun et al. 2012; Vemareddy et al. 2012b), where a couple of bipolar spots emerge, aligning in the y-axis in between pre-emerged bipolar spots lying along the x-axis, where complex magnetic structure usually forms. Because of this specific distribution of flux regions, the classified magnetic configuration of the AR transforms from simple β to complex $\beta\gamma\delta$. However, during its evolution on the disk, only C-class flares are observed to originate from this AR. In Figure 1 (top row), we show the AR flux distribution by plotting vector magnetograms at three different times during the emergence period. The background image is the normal component of the magnetic field, which is overlaid with vectors (arrows) of the transverse field. We can notice the growing flux distribution, as well as their separating motion in time.

In the panels of the second row of Figure 1, we displayed the velocity field of flux motions in this AR. Horizontal motions (as yellow vectors) are overlaid on the vertical velocity ($V_{\perp\rm n}$). From the statistics of the histogram analysis, the magnitude of horizontal components ranges up to 0.8 km s^{-1}, whereas a vertical component distribution up to 0.65 km s^{-1} is noticed at present. Significant upflows are detected where flux emergence occurred, and downflows are also seen, mostly away from the sunspot centers. Horizontal velocity vectors identify the curly or vortex-like motions in approximately counterclockwise direction in the following sunspot patch from the middle of the observational sequence.

Using the vector magnetic field data and after following the procedure described in Section 2, we calculated helicity flux (Equation (6)) and energy flux (Equation (2)) in time, whose distribution maps, as an exemplary case at three different times, are displayed in Figure 1 (third and fourth rows). For the association of these fluxes with magnetic flux regions, contours of $B_{\rm n}$ at ± 120 G are overdrawn. As a note, we point out that the helicity flux densities are not gauge invariant; only the area-integrated relative helicity flux is gauge invariant. In order to define true helicity flux density, the coronal linkages need to be provided (Pariat et al. 2005). Therefore, the helicity flux densities obtained from tracked flow velocity that are shown in these panels may not be precisely accurate. With the limitations of not having coronal linkages, and for the purpose of our analysis interpretation, we nevertheless plot and refer to the localized distribution in this study. The values in the distribution of helicity are both positive and negative. We scaled these maps within $\pm 10^{19}\,Mx^2$ cm^{-2}s^{-1} for better visibility. It is clear that most of the AR (both positive and negative flux regions) is spread with negative values of helicity flux. Especially, central locations of sunspots have associated large values of helicity flux. Because of this, the AR flux system is expected to have dominant negative or left-handed chirality. However, any part of the flux system is subjected to transform from one-handedness to another by transferring helicity during the course of its evolution. The distribution of energy flux is in the range of $\pm 10 \times 10^9$ erg cm^{-2} s^{-1}, and these images are scaled within 10^9 erg cm^{-2} s^{-1}. It is worth pointing out that helicity and energy flux distributions are not identical in the same polarity regions. Specifically, the sign distribution is dominantly positive. It may be due to the fact that the energy flux is weighted with the normal component of velocity and transverse magnetic field, while they are normal components of magnetic flux and transverse velocity weighted in helicity flux. So, emerging regions and locations with strong horizontal magnetic field are likely to have large values of

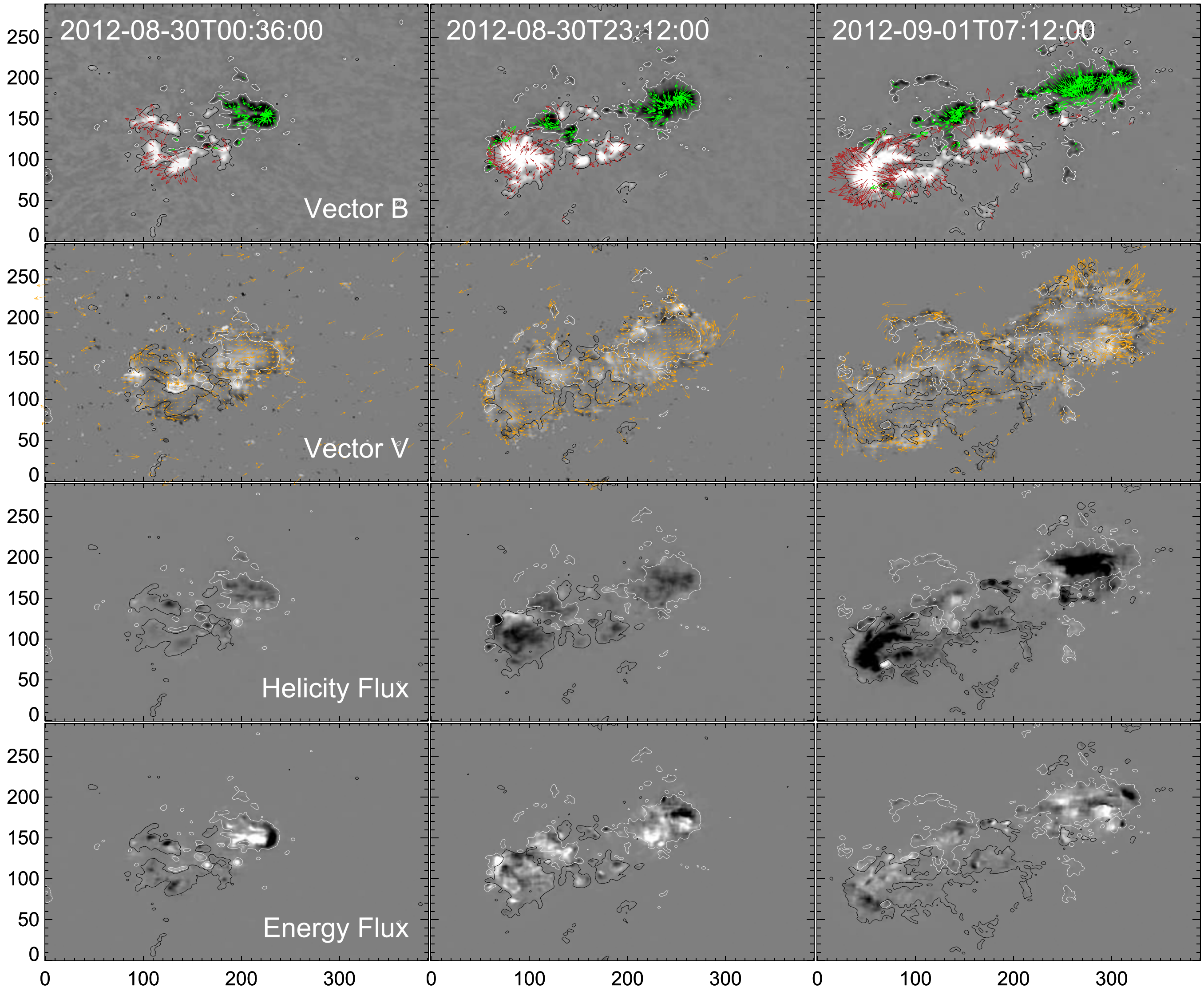

Figure 1. First row: vector magnetic field maps of AR 11560 at three different times during its emergence phase. The background image is the normal component of the magnetic field, and the red (green) arrows in the positive (negative) flux polarity regions refer to the direction of the transverse field. The length of the arrows is proportional to the magnitude of the transverse field. Second row: horizontal velocity vectors (yellow arrows) are overplotted on normal velocity maps of flux motions derived from DAVE4VM. The arrow lengths are normalized to a maximum magnitude of velocity of 0.8 km s^{-1}. Normal velocity maps are scaled within ± 0.4 km s^{-1}, where black (white) patches indicate downflows (upflows) of fluxes. Third row: helicity flux distribution ($G_\theta(x, y)$) in the AR corresponding to the panels in the first row. All maps are scaled within $\pm 1 \times 10^{19}$ Mx^2 cm^{-2} s^{-1}. Black (white) patches indicate negative (positive) helicity flux distribution. Fourth row: energy flux distribution maps corresponding to the panels in the first row. White (black) patches refer to positive (negative) distribution of energy flux. Scaling is done within $\pm 1 \times 10^9$ erg cm^{-2} s^{-1}. In all the panels, iso-contours of the normal magnetic field at ± 120 G (black/white) are overdrawn to identify the polarity regions and their association with the studied property. The field of view in each panel is indicated in pixels of 0.5 arcsec.

helicity flux and are major contributors to coronal energy content.

The time profiles of magnetic flux in AR 11560 are shown in the top panel of Figure 2. Positive flux is an integrated quantity of flux from north polarity, and negative flux is that from south polarity. To avoid background flux, which is due to noise, we accounted for $|B_z|$ values having 50 G and above in the computation of flux. The flux profile increases from 2×10^{22} Mx^2 on August 29 to $9.5 \times 10^{22} Mx^2$ by the middle of September 4. It can also be noticed from these profiles that the values in the flux profiles from north and south polarity have slightly different magnitudes, which explains the imbalance of the flux content (5%) in the AR. Since the AR is well within the field of view that contains conjugate footpoints of field lines from a polarity region, which is a necessary condition for the accurate assessment of energy and helicity fluxes, we attribute the observed imbalance of the fluxes to either measurement limitations or errors. Evidently from the plot, the net quantity of unsigned flux monotonously increases, signifying the flux emergence scenario and the value reached to 19×10^{22} Mx^2.

Time evolution of helicity flux is shown in the middle panel of Figure 2. We spatially integrated the helicity flux density due to the shear term ($\boldsymbol{V}_{\perp\mathrm{t}}$) and emergence term ($V_{\perp\mathrm{n}}$) separately. The shear term is dominant in the overall time period over the emergence term, both of which are negative. The shear term started with a value of $-0.5 \times 10^{37} Mx^2$ s^{-1} at the instance of emergence of bipoles and reached a maximum value of $-5.5 \times 10^{37} Mx^2$ s^{-1} by the first quarter of September 1. Thereafter it decreased to its starting value by September 4. The

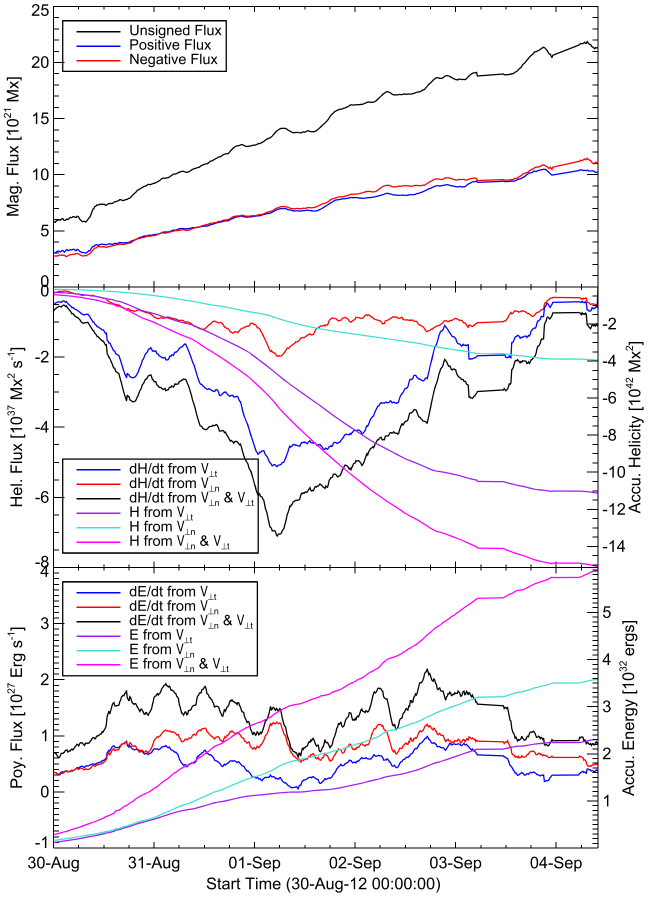

Figure 2. Time evolution of magnetic flux, helicity, and energy fluxes in the AR 11560. Top: time profiles of line-of-sight flux from north (blue) and south (red) polarity regions in the AR. Net unsigned flux is also plotted (black). The monotonic increase of fluxes with time indicates the emergence scenario of the AR. Middle: time profiles of the helicity flux injection rate (Equation (1)) plotted separately for shear (blue) and emergence (red) terms. The net ($V_{\perp t}$ term plus $V_{\perp n}$ term) profile is plotted in black. The corresponding accumulated values of coronal helicity (H) as a function of time are plotted with the *y*-axis scale on the right. Bottom: time profiles of energy flux injection rate (Equation (2)) plotted separately for shear (blue) and emergence (red) terms. Their net profile is also shown in black. The corresponding accumulated coronal energy (E) budgets with time are also plotted with the *y*-axis scale on the right.

energy flux profile also has a similar trend, but values are smaller by a factor of five. The net profile of the helicity injection rate from the combination of the shear and emergence terms is also shown in the same panel. Moreover, these profiles are integrated over time to estimate the accumulated quantities ($H_{\rm accu} = \int_0^T \frac{dH}{dt} dt$) as an estimate to coronal helicity fluxes and are shown in the same panel. From the plot, the total coronal helicity ($-15 \times 10^{42}\, Mx^2$) is mostly contributed by the shear term ($-11 \times 10^{42} Mx^2$), which is higher than the emergence term ($-4 \times 10^{42}\, Mx^2$) by a factor of three.

Similarly, the evolution of energy flux with time is shown in the bottom panel of Figure 2. This profile shows short-term fluctuations along with variations at a timescale of 12 hr, probably related to the orbital velocity of HMI. The noise in the inverted magnetic field is due to many factors (Hoeksema et al. 2014). One of them is the orbital velocity (± 3 km s^{-1}) of HMI, which introduces temporal and spatial variations of inverted magnetic field over a period of 12 hr as reported in a few recent studies (Hoeksema et al. 2014). Contrary to helicity flux profiles, the values of the energy flux profile are positive, and the emergence term is dominated over the shear term in the overall time duration. Positive profiles of the energy fluxes are consistent with the dominant positive distribution as in Figure 1. Both shear and emergence profiles exhibit increasing behavior in the first 20 hr of the observation, which includes flux tube emergence. To avoid short-duration fluctuations due to noise in the vector magnetic field, we applied a 3 hr running average to all the time profiles. The coronal energy budget is estimated by time integrating ($E_{\rm accu} = \int_0^T \frac{dE}{dt} dt$) these profiles of energy flux injection. The accumulated energy with time is plotted in the same panel with the *y*-axis scale on the right. As we can notice from the plot, the net value of coronal energy (6×10^{32} erg) is a combination of shear term contribution (2.4×10^{32} erg) and emergence contribution (3.6×10^{32} erg).

4. AR 11726

This AR is recognized to be emerging from 2013 April 19 on the solar disk location E16°N13°. Within a period of a day, it emerged rapidly, forming well-appearing sunspots. The leading polarity is negative and following polarity is positive sunspot. The AR further grows to apparently complex flux distribution, and after four days it appears to consist of a leading negative flux in the form of a major sunspot and following positive flux as plage group regions. The flux distribution of this AR as vector magnetograms at different epochs of time is depicted in the top row of Figure 3. Strong horizontal field is seen distributed within a big sunspot patch at the center of the AR. During the period of our study, this AR is found to be the source region of 52 C and 1 M-*GOES* class flares, reflecting its highly transient activity.

Vector velocities of tracked flux motions are shown in the second row of panels of Figure 3. While the AR is evolving to grow bigger, leading and following flux patches move in opposite directions, and flux is emerging from the center of the AR. Contours of normal magnetic flux are also shown to identify the flux regions with respect to the normal velocity map. These maps show both upflows and downflows in any cross section of flux tubes. Most outflows are noticed at the peripheral regions of sunspots, which are likely driven by upflows at the emerging locations. Maximum horizontal and vertical velocities detected are 0.85 and 0.6 km s^{-1}, respectively. These values are believed to be reasonable under the slow evolution conditions of typically 1 arcsec displacements within a duration of 12 minutes.

Distribution of helicity flux (both $V_{\perp t}$ and $V_{\perp n}$ terms) of this AR is depicted in Figure 3(third row). Positive- and negative-signed values of helicity flux at different magnitudes are noticed to spatially distribute over the AR. The sign distribution over any polarity flux patch is changing over time. The typical values of shear and emergence helicity fluxes are within $\pm 10 \times 10^{19}\, Mx^2$ cm^{-1}s^{-1}, where the emergence term values are smaller in magnitude compared to the shear term. Therefore, when adding these two terms, the resultant value is dominated by the shear term value in the locations of strong normal magnetic field and horizontal velocity as can be observed from these panels. Intense distribution of positive helicity flux is mostly associated with the positive sunspot patch at the middle of the AR. Similarly, the energy flux distribution of this AR is plotted in the bottom panels of Figure 3. The values range to a maximum of

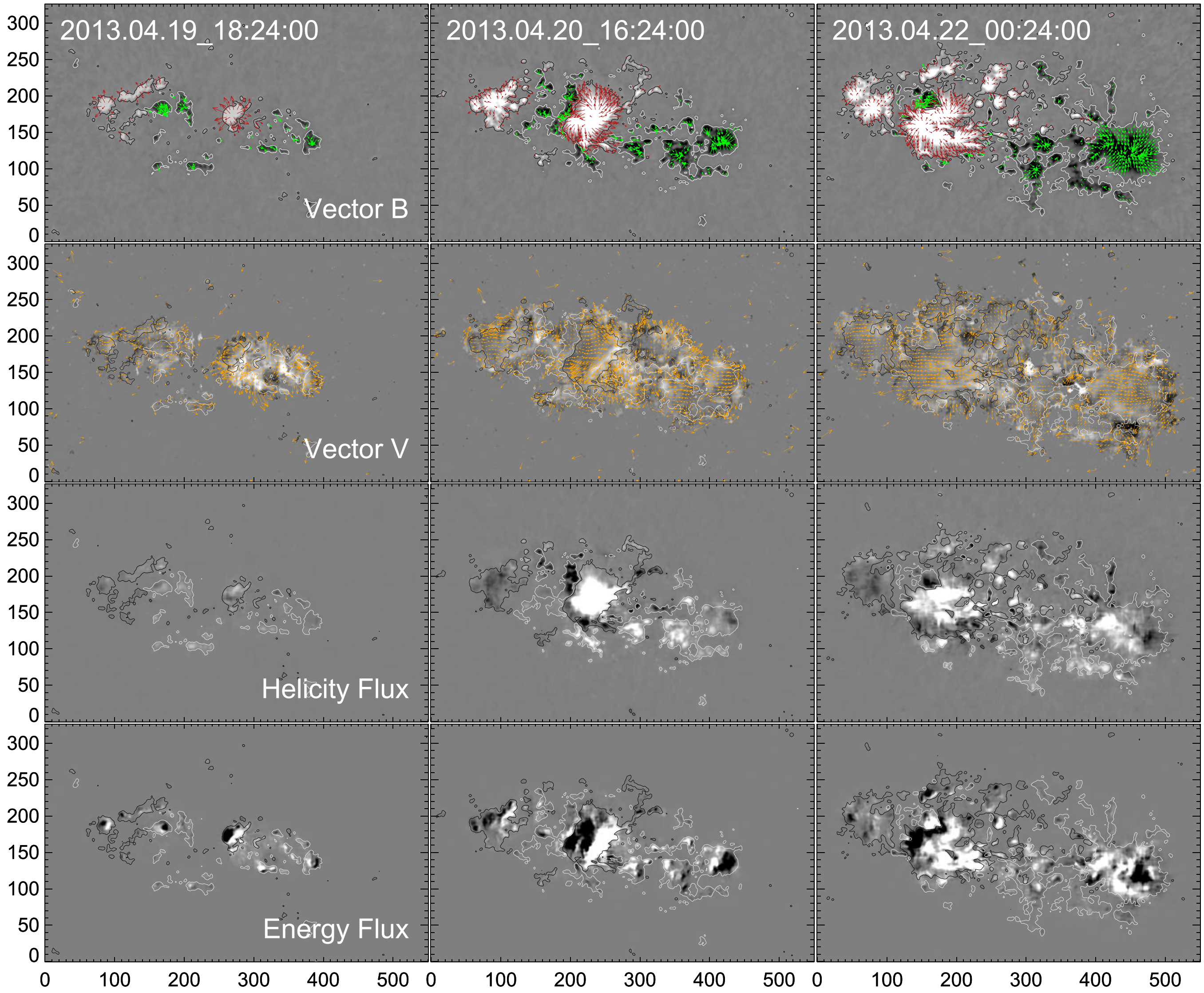

Figure 3. Same as Figure 1 but for AR 11726.

$\pm 9 \times 10^{9}$ erg $\text{cm}^{-2}\,\text{s}^{-1}$. All these maps refer to surface distribution of energy and helicity fluxes, while the magnetic structure is protruding the photosphere from below in the successive stages of observations.

The time evolution of magnetic helicity and energy fluxes are plotted in Figure 4, which are obtained by integrating their distribution over the surface at every instance of time. The imbalance of magnetic fluxes is up to 8%, which is well within the noise level of observations. The flux content starts at $1 \times 10^{21}\,Mx^2$ and reaches $20 \times 10^{21} Mx^2$, which reveals the gradual increase of flux content by expansion of flux tubes after their rapid emergence phase. The helicity flux curves reveal the dominant positive distribution, which reflects dominant right-handed chirality of the flux system in the AR. A 3 hr running average is applied to the obtained profiles. The shear term helicity flux input is dominated over the emergence term. Intense injection of helicity flux associated with the shear term at the central sunspot location raises the profile over the first 1.5 days. Later it remained with undulations for a half-day period, followed by a rapid increase of more than 100%, and then dropped by the same amount in the later half day. During this period of 3.83 days, a total of $18 \times 10^{42} Mx^2$ is being accumulated, of which 22% is contributed by the emergence term and 78% is supplied by the shear term.

As the magnetic flux starts emerging, the vertical flow drives horizontal flux motions, which contribute to input both magnetic energy and helicity flux. From the time profile of the energy flux, it is clear that significant input from both terms is mainly dominated by emergence, in the first 1.5 days. In the later phases, the flux emergence and horizontal motions of expanding flux tubes both contribute to energy input, as the shear and emerging terms have comparative values of energy flux. Owing to these time profiles of energy flux, the coronal content of energy would likely be 9×10^{32} erg, which is having approximately equal shares of emergence and shear terms.

5. AR 11928

This AR comes into existence starting from December 16 at the location of the solar disk E40°S15°. Initially it appeared to have two opposite-polarity flux regions. Both the leading positive and following negative polarities display apparent translational motions while emerging. Within a day later, they

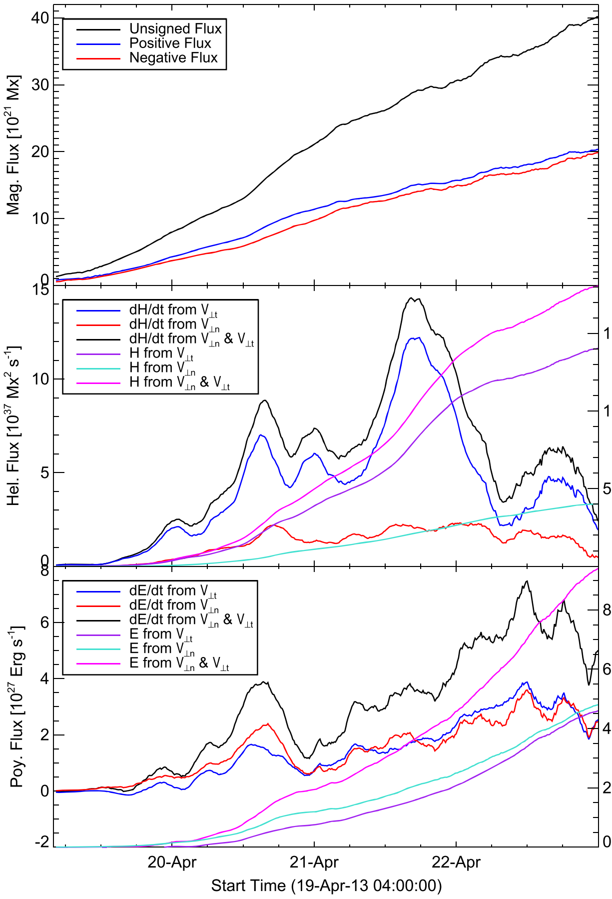

Figure 4. Same as Figure 2 but for AR 11726.

grow to form a full-fledged AR with well-formed leading positive sunspot and following negative-polarity group regions. We show the vector magnetic field maps of this AR at three different times in Figure 5 (first row). As one can notice, during the considered time interval, the magnetic configuration evolved from simple β to complex $\beta\gamma$. Flaring activity from this AR is limited to *GOES* class C. Snapshots of corresponding vector velocities, helicity, and energy fluxes are displayed in the second, third, and fourth row of panels of Figure 5, respectively. Upflows are detected at the center of the AR corresponding to flux emergence. Statistics of flow velocity are similar to the previous two ARs, distributed to a maximum of 0.8 km s^{-1}. In the course of evolution of flux motions, the leading positive polarity is seen to be associated with changing sign of helicity flux distribution, particularly in the shear term. Initially it has a distribution of negative flux, which slowly evolved to intense positive flux by the middle of December 17. In the later phase, this distribution evolved to intense negative helicity flux by the early period of December 19. As the shear term is involved with transverse motions, and as we observed that these velocity vectors appear to have a rotating pattern of motions in the counterclockwise direction around that large sunspot region (see last panel of second row, Figure 5), it is very likely that the flux tubes have a negative helicity pattern as noticed here.

The time profile of magnetic fluxes notifies significant imbalance of the flux (Figure 6). Because the AR lies near the east limb, the projection effects, together with noise, make it difficult to identify the emerging bipoles. Even the threshold of 50 G could not remove background fields, which contribute much to the observed imbalance of fluxes. As we can see from the figure, the contour levels of 120 G isolate the regions well, which emphasizes that the chosen field of view includes the bipoles of the AR flux. The profile of coronal helicity budget reveals peculiar evolution. This is because the coronal helicity in the first half of time comes from the positive input of shear helicity flux, which is subsequently supplied by negative input (see Figure 5) in the later half. Note that the emergence term budget is less significant, which is positive due to the supply of positive input of helicity flux in the entire time period. The injection rate of energy flux is strong during the AR emerging phase of the first 15 hr. Thereafter, both $V_{\perp t}$ and $V_{\perp n}$ term profiles vary with significant undulations at comparable values. On time integration, the coronal energy budget amounts to 6×10^{32} erg, which is accumulated by shear and emergence terms in approximately equal portions. This case is different from those studied in Liu & Schuck (2012), with coronal energy dominantly contributed by the $V_{\perp n}$ term.

6. FLUX EMERGENCE VERSUS ACCUMULATION OF HELICITY AND ENERGY FLUXES

The time profiles of helicity and energy fluxes can also be interpreted with respect to emergence of flux and its evolution. We plot accumulated (time-integrated) quantities of helicity and energy flux as a function of net absolute magnetic flux in Figures 7 and 8. The flux content in AR 11726 is approximately twice that in AR 11560. In these two ARs, the helicity accumulation from the emergence term is increasing monotonically with the increase of respective magnetic flux content. The shear term coronal helicity budget is small until the magnetic regions form and grow to $5 \times 10^{21}\,Mx$, from where it increases in a quadratic fashion with further growth of magnetic flux. In other words, after the main flux emergence phase, there is a great amount of shear term helicity accumulation from a small increase of magnetic flux. Therefore, these curves delineate the necessity of flux emergence primarily, which drives thereupon the surface motions that are significantly contributing to coronal helicity buildup. Our interpretations are consistent with the conclusions of Vemareddy et al. (2012b, see their Figure 12), arrived at with the assumption that flux transport velocity is valid (Démoulin & Berger 2003). They found that a smaller amount (<25%) of helicity comes from a greater amount (more than 75%) of magnetic flux in AR 11158, in contrast to a major amount (<75%) of helicity being associated with a little amount (10%) of magnetic flux content.

AR 11928 has specific evolving conditions of magnetic fluxes that are different from that in the rest of the ARs here. As the time profile of the helicity flux rate turns from a positive value to negative value, its accumulation in the corona is positive in the first half time, which is depleted with added negative amounts in the later half time. Mostly this change is due to the dominant shear term of helicity flux, which is seen to be associated with the leading large sunspot (see Figure 5) of north polarity. In contrast to the emergence term, the shear term exhibits similar evolution to AR 11560 and AR 11726, showing steep buildup well after the AR emergence and having a net flux of $6 \times 10^{21}\,Mx$ in each polarity.

On the other hand, it is the emergence term that dominates the contribution of the coronal energy budget over the shear term. Emergence of twisted flux tubes during flux

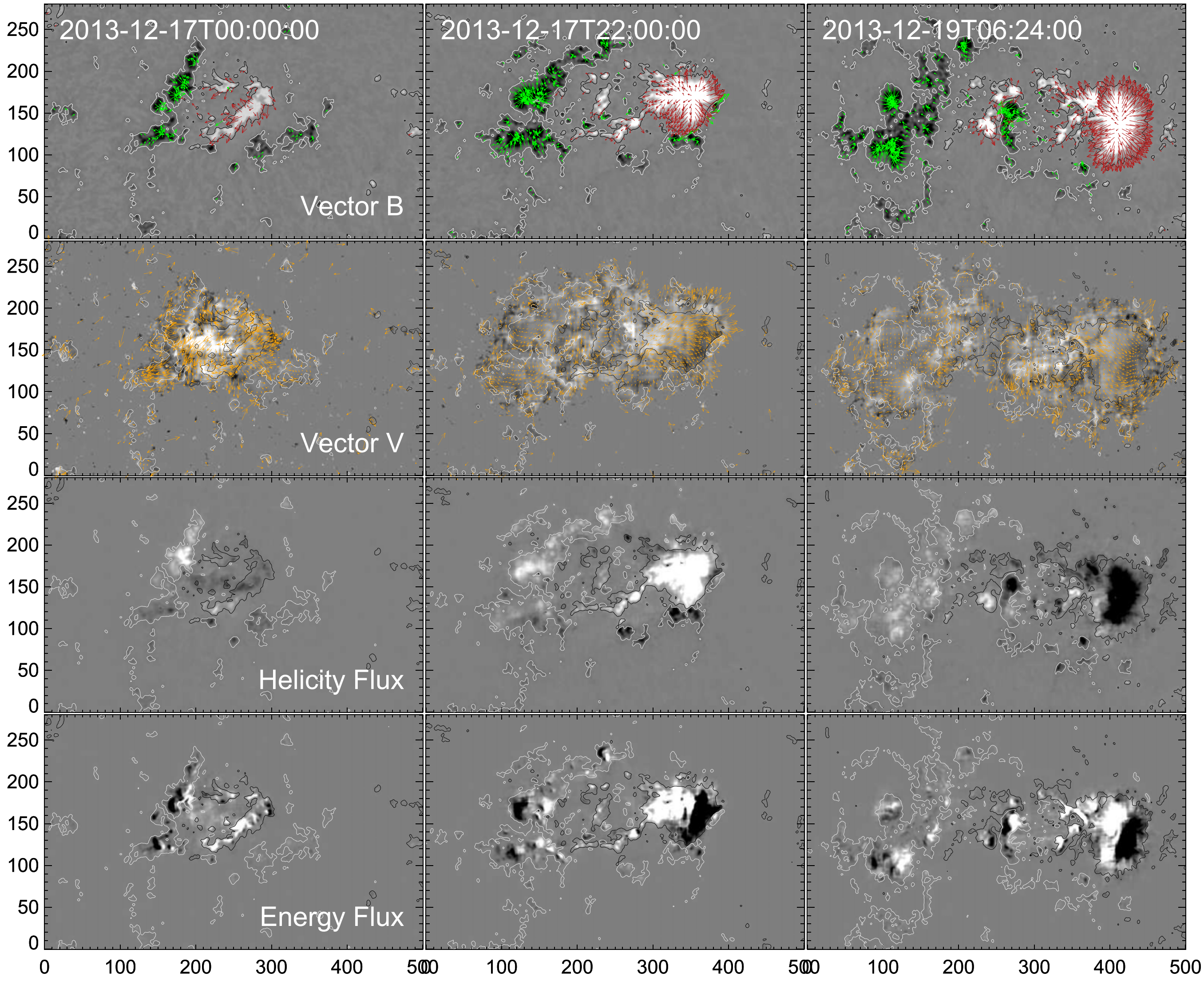

Figure 5. Same as Figure 1 but for AR 11928.

emergence injects significant energy, whereas after emergence the shear motions twist the flux tubes, which results in the quantitative measure of the shear term. All of these plots will give a coherent understanding of which term played a significant role in the buildup of coronal energy and helicity budget when seen from the magnetic flux perspective. For a quantitative analysis, we can follow the same interpretations in Vemareddy et al. (2012b) that how much of these terms of shear and emergence change the coronal budget of helicity and energy by a change of particular boundary magnetic evolution. For example, in AR 11726, for an increase of magnetic flux from $5 \times 10^{21}\,Mx$ to $15 \times 10^{21}\,Mx$, the shear helicity change that took place is about $12 \times 10^{42}\,Mx^2$; however, it is only $3.5 \times 10^{42}\,Mx^2$ for the emergence term. These plots evidently demonstrate that the magnetic helicity comes from twisted magnetic flux tubes emerging from the solar interior and is generated by shearing and braiding of field lines identified by tangential flux motions. In addition, these plots also provide details on the relative buildup of these terms with respect to emerging and expanding flux in the AR.

In order to quantify the phase lag of shear helicity flux with respect to magnetic flux, we follow a similar procedure to that in Liu & Schuck (2013). For that, essentially we correlate the normalized values of the change rate of the total unsigned flux and the helicity fluxes, by shifting the latter in a search for a maximum value of correlation. A 3 hr running average is applied to the time profiles of helicity flux to reduce the fluctuations arising from taking the derivative. The shear helicity flux is found to have a phase delay of 6, 14, and 5 hr with respect to the unsigned flux in AR 11560, AR 11726, and AR 11928, respectively, whereas the delay of emergence helicity flux is less significant, limited to about 1–2 hr.

7. ENERGY AND HELICITY INJECTION FROM UPFLOWS AND DOWNFLOWS

The emergence helicity and energy flux are separated into two components: one from upflows $(+V_{\perp n})$ and one from downflows $(-V_{\perp n})$. These are plotted in Figures 9–11 for AR 11560, AR 11726, and AR 11928, respectively. Note that the helicity flux is a meaningful physical quantity only when integrated over an area containing conjugate footpoints of magnetic structure above the boundary surface. Here the separation over positive and negative vertical velocity is strictly prohibited; however, to get a general idea, we plot them

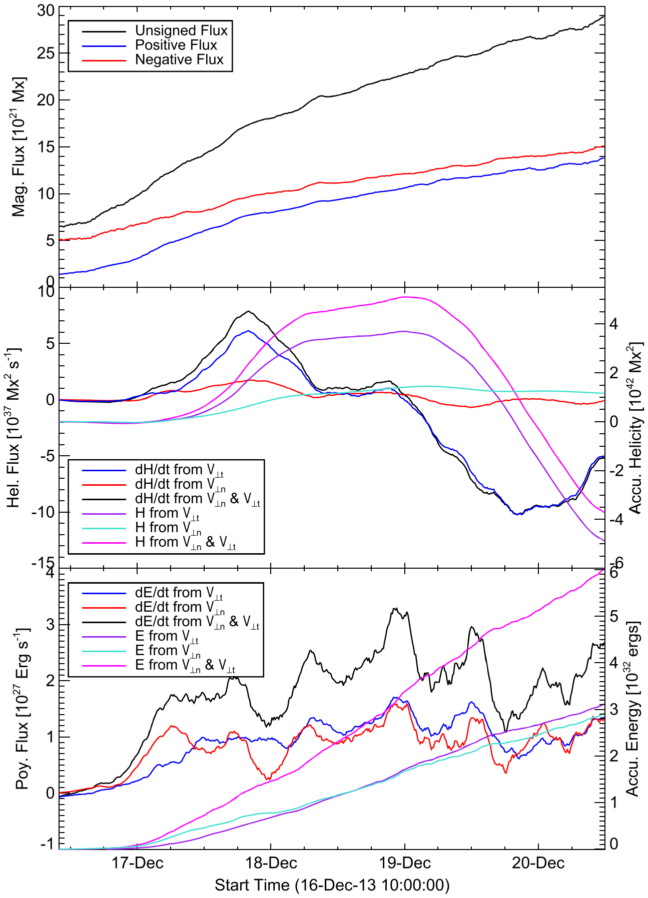

Figure 6. Same as Figure 2 but for AR 11928.

additionally with the net helicity flux value. The upflow helicity flux in AR 11560 varies from near zero to a maximum of $2.5 \times 10^{37} Mx^2$ s^{-1} and then evolves back to a near-zero value, which resembles the profile of shear helicity flux, as found in two ARs by Liu & Schuck (2012). The downflow flux exhibits variations around zero value without a significant trend. In AR 11726, both the upflow and downflow helicity fluxes increase monotonically according to the emerging flux until 2013 April 21, from where they evolve with a mild increase. The upflow helicity flux is dominantly contributing to the net profile over the downflow flux. The helicity flux from upflow in AR 11928 evolves with substantial variation, where it has positive values in the first half and negative values in the latter half of the observation time. And the downflow flux varies with smaller magnitude at about zero level. From these plots, it is obvious that the dominant emergence helicity flux in an AR originates from upflow, and the downflow does not play a significant role while deciding the helicity pattern of the flow. The reason for why the dominant emergence helicity flux comes from upflow lies in the fact of the construction of vector potential ($\boldsymbol{A}_{\rm p}$) from a normal component of the magnetic field ($B_{\rm n}$) and the newly emanating twisted flux tubes ($\boldsymbol{B}_{\rm t}$). So, the presence of more twisted horizontal field contributes to this term. Importantly, horizontal vector orientation decides the chirality of flux tubes.

Time profiles of the upflow and downflow energy flux in the three ARs are opposite in sign and comparable in magnitude. Both of them start from zero and increase with the emergent increase of magnetic flux. After the rapid emergence phase, these profiles almost retain their level of evolution. Note that the net profile is always positive in the three AR cases. As the emergent energy flux cannot be negative, the dominant contribution of energy flux comes from upflow. Moreover, we found the distribution of normal flow velocity to follow Gaussian, which has a rising amplitude with emerging flux in the ARs. As the square of the horizontal field magnitude is a positive quantity, the expression of emergent energy flux yields opposite-signed values from the upflow and downflow regions. Therefore, locations with strong horizontal fields (not necessarily twisted) play key roles with this term. For the emergent energy flux quantity to be positive, its input should dominantly come from the upflow, which has to be the case in emerging flux regions.

The results in the three AR cases summarily demonstrate that the upflows play an unambiguous role in injecting energy and helicity flux into the corona, as also predicted by numerical simulations (e.g., Fan & Gibson 2003; Magara & Longcope 2003; Manchester et al. 2004; Cheung et al. 2010).

8. DISCUSSION

The magnetic energy and helicity in the AR are two important parameters for a quantitative study of magnetic origins of solar eruptions. The field lines in the closed magnetic structure in the corona have footpoints rooted in the photospheric boundary. Therefore, during AR emergence and their evolution, the lower boundary acts as the driver of the evolution in the structure either via boundary flows or via the injection of an additional structure through it. Consequently, the magnetic helicity in the corona can be transported either to or from the structure through this boundary, or it can be generated by flows on the boundary. Based on these arguments, Berger & Field (1984) derived a surface integral expression for the temporal variation of the relative magnetic helicity in a magnetic configuration. A similar expression for the magnetic energy has been derived (Kusano et al. 2002; Schuck 2006) as Equation (2). Both the expressions for energy and helicity injection have dependence on magnetic field vectors and the boundary flows. By integrating these expressions over time, the total budgets of coronal energy and helicity are possible to estimate.

Alternatively, one can also estimate the coronal budgets of these quantities by the volume integral of these densities derived from magnetic field observations in the corona. As of now there are no routine coronal magnetic field measurements available; the boundary field measurements are being exploited for their construction in the corona by an appropriate assumption presumably force-free (zero Lorentz force; e.g., Wiegelmann 2004; Vemareddy & Wiegelmann 2014). Because the lower boundary observations are not force-free, there is a possibility that sometimes the model field may not represent realistic structure in the corona and therefore the consequent estimates of energy and helicity, although involving time consuming immense calculations, may not be exact. Therefore, provided better cadence and high-resolution magnetic field observations, the coronal estimates of energy and helicity from expressions (1) and (2) are practically easy and reliable as they do not explicitly require force-free fields. However, one has to look into detailed discrepancies between the above two approaches on these estimates, which is our future task.

Numerical simulations of emerging flux tubes predict the expansion of flux tubes after they penetrate the photosphere

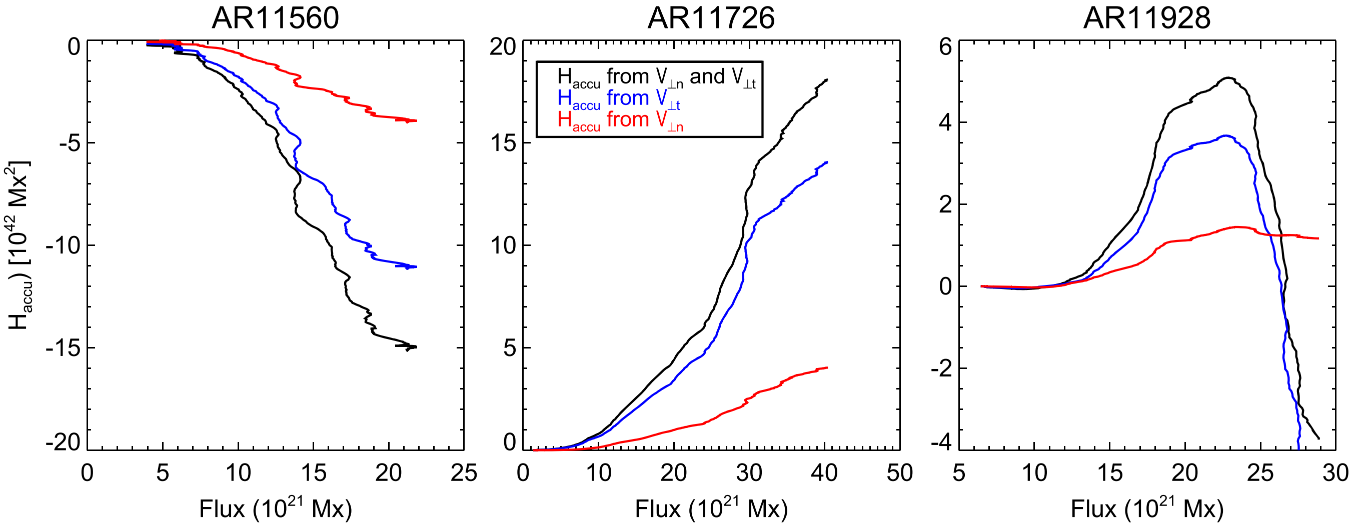

Figure 7. Helicity accumulations in the corona as a function of photospheric absolute net magnetic flux in AR 11560, AR 11726, and AR 11928. The helicity flux budget is computed from the shear ($V_{\perp t}$, blue) and emergence ($V_{\perp n,}$ red) terms separately and plotted in each panel.

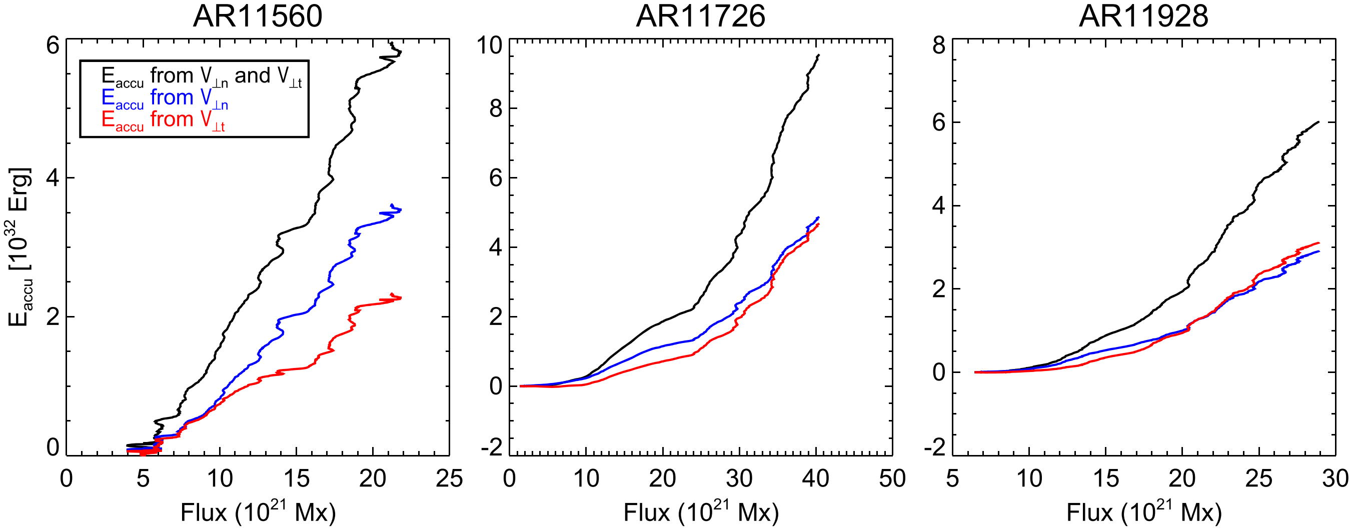

Figure 8. Energy accumulations in the corona as a function of photospheric absolute net magnetic flux in AR 11560, AR 11726, and AR 11928. The energy flux budget is computed from the shear ($V_{\perp t}$, red) and emergence ($V_{\perp n}$ blue) terms separately and plotted in each panel.

(Magara & Longcope 2003). During the early phase of emergence, the emerging (upward) motions play a dominant role in injecting energy and helicity. As flux emergence gets saturated, the polarity regions deform and fragment by shearing motions, which play a predominant role in energy and helicity injection. The observational results of the ARs have many similar findings to the simulations. The observations reflect having a significant emergence term contribution from upflow helicity and energy throughout the period of evolution, with a fast rate of injection in the early emergence phase. Specifically, our analysis results are found to have energy flux injection in comparative speeds from both shear and emergence terms (Figures 4 and 6), which was found to dominantly come from the emergence term in earlier studies (Liu & Schuck 2012).

Identifying the relation of helicity, energy with the eruptive activity is very important to space weather, which requires high-quality observations as input to theoretical predictions. We seek for characteristic evolving conditions of helicity and energy flux of AR under which most eruptions will be triggered. The three studied ARs distinguish those conditions of helicity flux where monotonic positive, negative, and mixed signs of flux are being accumulated (see Table 1). We attended to the activity scenario in the AR, by monitoring AIA 193 Å and LASCO C2 images simultaneously.[1] In AR 11560 (around 01/07:48, 02/04:00, 03/15:24 in 2012 September) and AR 11726 (around 20/08:00, 22/09:48UT in 2013 April) strong eruptions significantly disturbed the ambient atmosphere. Flares of different magnitude up to M-class level also occurred in these ARs. However, there were no strong eruption events noticed to launch from AR 11928, except flares of C-class level.

Monotonic input of helicity flux originates from magnetic regions evolving with rotating flow patterns (Vemareddy et al. 2012a, 2012b), which are well detected by DAVE4VM. When the corona is overaccumulated with helicity, the occurrence of CMEs is the only way to expel the helicity and field according to the conservation principle (Zhang &

---

[1] We made use of the CME list and associated movies at http://cdaw.gsfc.nasa.gov/CME_list/.

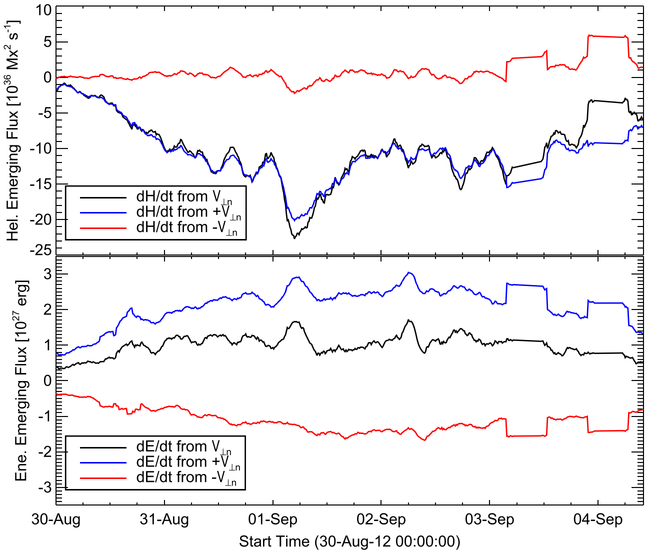

Figure 9. Emerging term evolution of helicity and energy flux in AR 11560. Top: time evolution of the $V_{\perp n}$ term of helicity flux (in black), which is computed for upflows ($+V_{\perp n}$ in blue) and downflows ($-V_{\perp n}$ in red). Note that dominant helicity originates from upflow. Bottom: time variation of the $V_{\perp n}$ term of energy flux (in black), which is decomposed into contribution from upflows ($+V_{\perp n}$ in blue) and downflows ($-V_{\perp n}$ in red).

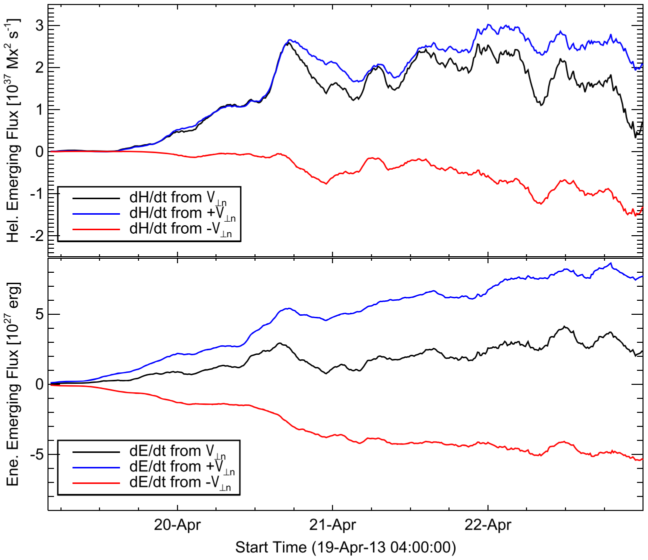

Figure 10. Same as Figure 9, but for AR 11726.

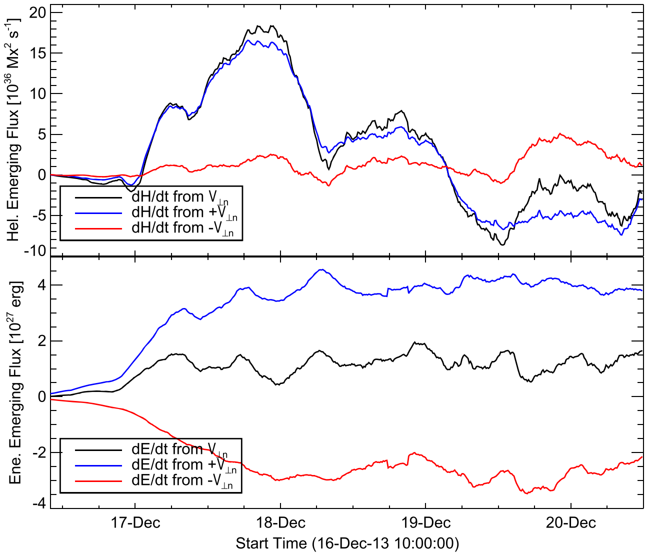

Figure 11. Same as Figure 9, but for AR 11928.

Low 2005). Therefore, such locations within the AR are capable to launch powerful CMEs. Another consequence of accumulation of helicity is formation of sigmoidal flux ropes, which are precursor configurations of eruptions. On the other hand, when positive and negative helicities coexist in a single domain, flux systems of opposite helicities can merge via reconnection, leading to magnetic helicity cancellation. When this process occurs, the reconnected field may relax toward a state with lower total helicity, so there is less minimum energy, and the field energy corresponding to magnetic helicity of mixed signs can be released (Kusano et al. 2004) via a flare. The sign change of the area-integrated net helicity flux implies such a scenario of flares with no strong eruptions, which is the case in AR 11928 over a period of days. Note that local changes of sign distribution also result in short time interval fluctuations in the time profile, which might include the effect of observational noise. Therefore, the above two issues of triggering flares and CMEs by tracking magnetograms of flux motions need a detailed investigation with the help of simultaneous observations of the corona. The above two scenarios of the helicity flux evolution are concurrent with the observed activity in the ARs, although there are many local factors that still need to be accounted for.

Having derived the energy and helicity fluxes, it would be interesting to explore the link between relative magnetic helicity and total magnetic energy. With the increase of relative magnetic helicity as a representative of the complex nature of the structure over a reference field, from general expectations, the free magnetic energy is supposed to build up. In Figure 12, we plot the accumulated relative helicity against the accumulated total energy in the three AR cases here, separately. Clearly, the buildup of energy takes place in a nonlinear fashion, and the negative helicity AR also had a positive quantity of energy. This curve in AR 11928 is due to positive accumulation of helicity until $5 \times 10^{42}\,Mx^2$, which is canceled by added negative flux and its accumulation. Therefore, this curve in itself is physically not meaningful unless its meaning is disclosed. All of these plots obviously disclose the buildup of energy in the AR magnetic structure corresponding to the development of relative magnetic helicity through footpoint motions and emergence of flux.

In a study, Georgoulis & LaBonte (2007) had explored the relation between free magnetic energy and relative magnetic helicity by splitting magnetic field into current free ($\boldsymbol{B}_{\rm p}$) and complex non-potential fields ($\boldsymbol{B}_c$), where the total energy (E) is related to relative magnetic helicity ($H_{\rm m}$) through

$$E = E_{\rm p} + \frac{\alpha}{8\pi} H_{\rm m} = E_{\rm p} + E_{\rm c} \tag{7}$$

with a constant of proportionality α as a linear force-free parameter. This means that the magnetic field line configuration is determined by a model of linear force-free assumption, which is different from and in a higher energy state than the simple potential field state. According to this expression, the

Table 1
Summary of the Analysis in the ARs

Property	AR 11560	AR 11726	AR 11928
Time	2012 Aug 30–Sep 04,	2013 Apr 19–22	2013 Dec 16–21
Disk position	N3	N13	S15
Accumulated helicity ($V_{\perp t}$,$V_{\perp n}$, $10^{42} Mx^2$)	−15 (−11, −4)	18 (14, 4)	−4 (−5, 1)
Accumulated energy ($V_{\perp t}$,$V_{\perp n}$,10^{32} erg)	5.9 (2.3, 3.6)	9.5(4.5, 5)	6 (3, 3)
Dominant chirality	Left	Right	Mixed

total energy of the system is a linear function of the sum of potential energy ($E_{\rm p}$) and the complex non-potential energy. In practice, for the evolving systems like the closed configurations of AR magnetic fields, both potential and non-potential energies vary with time in response to the evolving boundary observations.

In the cases here, the total energy E is increasing via a nonlinear curve with the increase of relative magnetic helicity (Figure 12). With this, the nature of the magnetic configuration is not tractable as potential energy included in the total energy is also varying. Very importantly, the total energy we inferred includes forces from non-magnetic origin (non-force free) at the photosphere, and therefore finding the relation between magnetic energy and helicity is not possible unless the field is constrained by an assumption that is probably force-free. For an approximated idea, we fit the curve with a straight line to find the slope (dotted lines in Figure 12). The model fits to data points in the curve are placed in each panel. Having the straight line model fit, the unknown potential energy $E_{\rm p}$ is determined by *the* y-intercept and the slope represents the value of $\alpha/8\pi$.

AR 11560 possessed an overall negative twist parameter $\alpha= 8.3 \times 10^{-8}$ m^{-1} with initial potential energy $E_{\rm p} = 0.44 \times 10^{32}$ erg. It is the positive twist that describes the approximated field configuration at $\alpha = 11.0 \times 10^{-8}$ m^{-1} in AR 11726 having the lowest potential energy of $E_{\rm p} = -0.18 \times 10^{32}$ erg. As explained earlier, the nonlinear curve of AR 11928 is unphysical, and so is its fit. In a similar way to the other two ARs, the energy and helicity relation in this AR can be understood by two separate line fits defined by positive alpha from (0–5) $\times$ 10^{42} Mx^2 and a negative alpha for the later part. We should point out that the model of constant torsion parameter for all field lines having footpoints in a polarity is a simple and easy representation of coronal magnetic fields. The disparity between the model fit and the original curve of energy and helicity accumulation may be resolved by invoking more realistic nonlinear force-free fields. Nevertheless, our intuitive model fit to the nonlinear curve of coronal energy and helicity accumulation obtained through flow velocity indeed yields typical α and $E_{\rm p}$ values and a reasonable relation between energy and helicity of coronal magnetic fields.

9. SUMMARY

Solar magnetic fields, together with their helicity, are created in the convection zone by various dynamo processes. These fields and helicity are transported into the corona through the solar photosphere and finally released into the interplanetary space via various energetic processes. In this connection, we studied, in this paper, the helicity and energy flux transport by following *three* emerging ARs. The major results of this study are as follows:

1. Flux emergence and their motions in the evolution of all emerging ARs are the origins of coronal energy and helicity flux. Dominant helicity flux from the shear term over the emergence term reveals the predominant role of the photospheric flux motions in the coronal helicity budget, while it is the emergence term that is dominant but still comparable to the shear term in the coronal energy content.
2. Flux emergence substantially brings both energy and helicity flux, which thereupon generates flux motions contributing predominantly to shear term, which is consistent with simulation of emerging flux tubes (Magara & Longcope 2003). Consequently, the shear helicity flux is found to appear with a phase lag (6, 14, 5 hr) with respect to absolute net magnetic flux. Both terms of net shear and emergence energy flux are always positive irrespective of helicity flux evolution.
3. The nature of helicity flux is decided by the pattern of evolution of fluxes in the ARs. From the two specific AR cases here (11560, 11726), the area-integrated net positive or negative helicity injection rate accumulates monotonic helicity in the corona, which is primarily due to the presence of uniform signed patches of helicity flux distribution. On the other hand, mixed-sign helicity flux patches or change of the sign of net helicity injection rate over time result in depleting the coronal helicity budget. These two distinguished types of helicity flux inputs from evolving fluxes at the photosphere lead to two important kinds of activity, viz., CMEs and flares according to present theoretical (Zhang & Low 2005; Zhang et al. 2013) and numerical (Kusano et al. 2004) concepts, as is observed here.
4. In the case of having no measurements and no appropriate model of coronal magnetic field, the relation of coronal energy and helicity can be reasonably explored by flow velocity of tracked vector magnetograms (Georgoulis & LaBonte 2007) at the photosphere. The curve of coronal energy and relative magnetic helicity identifies the nature of coronal magnetic fields. Within the practical limits, the structure of the coronal magnetic fields varies about the linear force-free configuration defined by a constant torsion parameter.

A careful study of evolution of helicity and energy flux in more emerging AR cases is expected to strengthen our results here. As we pointed out earlier, the helicity flux density is a gauge-dependent quantity; connectivity-based helicity flux maps are more reliable. Employing a force-free field extrapolation model, Dalmasse et al. (2013) corrected the helicity flux maps and found no significant difference in the distribution of the helicity flux pattern. A further specific investigation for the physical significance of the observed helicity flux pattern corresponding to flow velocity and its relevance to coronal activity in the AR is very much needed by the utilization of

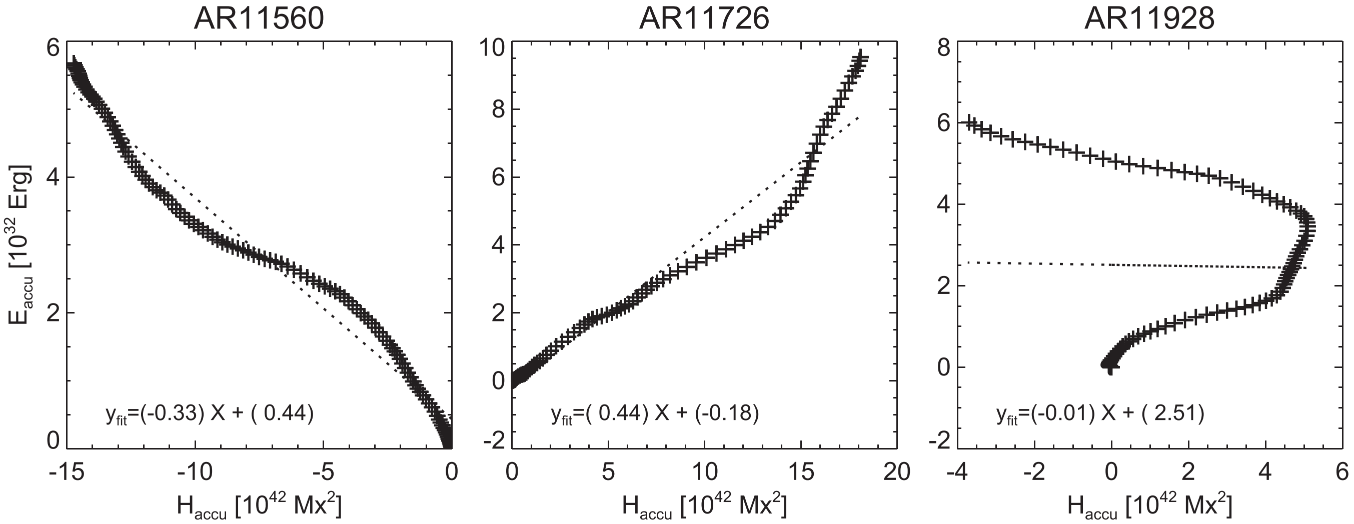

Figure 12. Variation of the total energy budget in the corona as a functional variation of helicity budget in AR 11560, AR 11726, and AR 11928. The dotted line having indicated slope and y-intercept in each panel refers to a straight line fit to the curve of variation of energy and helicity. The slope of this line indicates the constant torsion parameter $\alpha/8\pi$, and *the* y-intercept equals the potential energy ($E_{\rm p}$).

detailed coronal field line connectivity either from the observations or from the model. We intend to undertake such studies to explore more details.

The author thanks an anonymous referee for useful suggestions. The data have been used here courtesy of NASA/*SDO* and the HMI science team. We thank the HMI science team for making processed vector magnetograms available to the solar community. This work used the DAVE4VM code, written and developed by P. W. Schuck at the Naval Research Laboratory. The author expresses sincere gratitude to Y. Liu for his help in devising Equation (6). P.V. is supported by an INSPIRE grant under the AORC scheme of the Department of Science and Technology.

REFERENCES

Berger, M. A., & Field, G. B. 1984, JFM, 147, 133
Bobra, M. G., Sun, X., Hoeksema, J. T., et al. 2014, SoPh, 289, 3549
Borrero, J. M., Tomczyk, S., Kubo, M., et al. 2011, SoPh, 273, 267
Calabretta, M. R., & Greisen, E. W. 2002, A&A, 395, 1077
Centeno, R., Schou, J., Hayashi, K., et al. 2014, SoPh, 289, 3531
Chae, J. 2001, ApJL, 560, L95
Cheung, M. C. M., Rempel, M., Title, A. M., & Schüssler, M. 2010, ApJ, 720, 233
Choudhuri, A. R. 2007, AIP Conf. Ser. 919, Kodai School on Solar Physics, ed. S. S. Hasan & D. Banerjee (Melville, NY: AIP), 49
Choudhuri, A. R., Chatterjee, P., & Nandy, D. 2004, ApJL, 615, L57
Dalmasse, K., Pariat, E., Valori, G., Démoulin, P., & Green, L. M. 2013, A&A, 555, LL6
Démoulin, P., & Berger, M. A. 2003, SoPh, 215, 203
Fan, Y., & Gibson, S. E. 2003, ApJL, 589, L105
Finn, J. M., & Antonsen, T. M. 1985, COPPC, 9, 111
Forbes, T. G., Linker, J. A., Chen, J., Cid, C., et al. 2006, SSRv, 123, 251
Georgoulis, M. K., & LaBonte, B. J. 2007, ApJ, 671, 1034
Hoeksema, J. T., Liu, Y., Hayashi, K., et al. 2014, SoPh, 289, 3483
Jeong, H., & Chae, J. 2007, ApJ, 671, 1022
Klimchuk, J. A. 2001, in Space Weather, Vol. 125, ed. P. Song, H. Singer & G. Siscoe (Washington, DC: Am. Geophys. Un.), 143
Kusano, K., Maeshiro, T., Yokoyama, T., & Sakurai, T. 2002, ApJ, 577, 501
Kusano, K., Maeshiro, T., Yokoyama, T., & Sakurai, T. 2004, ApJ, 610, 537
Leka, K. D., Barnes, G., Crouch, A. D., et al. 2009, SoPh, 260, 83
Lin, J., Soon, W., & Baliunas, S. L. 2003, NewAR, 47, 53
Liu, Y., & Schuck, P. W. 2012, ApJ, 761, 105
Liu, Y., & Schuck, P. W. 2013, SoPh, 283, 283
Longcope, D. W. 2004, ApJ, 612, 1181
Magara, T., & Longcope, D. W. 2003, ApJ, 586, 630
Manchester, W., IV, Gombosi, T., DeZeeuw, D., & Fan, Y. 2004, ApJ, 610, 588
Maurya, R. A., Vemareddy, P., & Ambastha, A. 2012, ApJ, 747, 134
Metcalf, T. R., Jiao, L., McClymont, A. N., Canfield, R. C., & Uitenbroek, H. 1995, ApJ, 439, 474
Nindos, A., Zhang, J., & Zhang, H. 2003, ApJ, 594, 1033
November, L. J., & Simon, G. W. 1988, ApJ, 333, 427
Pariat, E., Démoulin, P., & Berger, M. A. 2005, A&A, 439, 1191
Park, S.-h., Chae, J., & Wang, H. 2010, ApJ, 718, 43
Priest, E. R., & Forbes, T. G. 2002, A&ARv, 10, 313
Schou, J., Scherrer, P. H., Bush, R. I., Wachter, R., et al. 2012, SoPh, 275, 229
Schuck, P. W. 2005, ApJL, 632, L53
Schuck, P. W. 2006, ApJ, 646, 1358
Schuck, P. W. 2008, ApJ, 683, 1134
Sun, X., Hoeksema, J. T., Liu, Y., et al. 2012, ApJ, 748, 77
Vemareddy, P., Ambastha, A., & Maurya, R. A. 2012a, ApJ, 761, 60
Vemareddy, P., Ambastha, A., Maurya, R. A., & Chae, J. 2012b, ApJ, 761, 86
Vemareddy, P., & Wiegelmann, T. 2014, ApJ, 792, 40
Webb, D. F., & Howard, T. A. 2012, LRSP, 9, 3
Welsch, B. T., Fisher, G. H., Abbett, W. P., & Regnier, S. 2004, ApJ, 610, 1148
Wiegelmann, T. 2004, SoPh, 219, 87
Yamamoto, T. T., Kusano, K., Maeshiro, T., Yokoyama, T., & Sakurai, T. 2005, ApJ, 624, 1072
Yamamoto, T. T., & Sakurai, T. 2009, ApJ, 698, 928
Zhang, M. 2013, in IAU Symp. 294, ed. A. G. Kosovichev, E. de Gouveia Dal Pino & Y. Yan (Paris: IAU), 505
Zhang, M., & Low, B. C. 2005, ARA&A, 43, 103